

# Bayesian model selection for testing the no-hair theorem with black hole ringdowns

S. Gossan, J. Veitch, and B. S. Sathyaprakash

*School of Physics and Astronomy, Cardiff University, 5, The Parade, Cardiff, UK, CF24 3YB*

(Dated: October 29, 2018)

In this paper we examine the extent to which black hole quasi-normal modes (QNMs) could be used to test the no-hair theorem with future ground- and space-based gravitational-wave detectors. We model departures from general relativity (GR) by introducing extra parameters which change the mode frequencies or decay times from their values in GR. With the aid of Bayesian model selection, we assess the extent to which the presence of such a parameter could be inferred, and its value estimated. We find that it is harder to measure the departure of the mode decay times from their GR values than it is with the mode frequencies. The Einstein Telescope (ET, a third generation ground-based detector) could detect departures of as little as 8% in the frequency of the dominant QNM mode of a  $500 M_{\odot}$  black hole, out to a maximum range of  $\simeq 6$  Gpc ( $z \simeq 0.91$ ). The New Gravitational Observatory (NGO, an ESA space mission to detect gravitational waves) can detect departures of  $\sim 0.6\%$  in a  $10^8 M_{\odot}$  black hole to a luminosity distance of 50 Gpc ( $z \simeq 5.1$ ), and departures of  $\sim 10\%$  in a  $10^6 M_{\odot}$  black hole to a luminosity distance of  $\simeq 6$  Gpc. In this exploratory work we have made a specific choice of source position (overhead), orientation (inclination angle of  $\pi/3$ ) and mass ratio of progenitor binary ( $m_1/m_2 = 2$ ). A more exhaustive Monte Carlo simulation that incorporates progenitor black hole spins and a hierarchical model for the growth of massive black holes is needed to evaluate a more realistic picture of the possibility of ET and NGO to carry out such tests.

PACS numbers:

## I. INTRODUCTION

Merging compact binaries consisting of neutron stars or black holes are promising sources [1] of gravitational radiation for advanced gravitational wave detectors that are currently being built [2, 3]. These sources are also potential laboratories for testing general relativity (GR) in the strong field regime [4–8]. The result of such an event (with sufficiently massive progenitors) is a highly perturbed black hole (BH) which rapidly returns to its quiescent state (i.e., a Kerr BH [9]), through the emission of gravitational waves (GWs). The perturbation, and therefore the emitted radiation, can be expanded in the natural basis of oscillations, the quasi-normal modes (QNMs) [10] (for a recent review on QNM see, e.g., [11]). A Kerr black hole is characterised only by its mass and angular momentum, and so are the complex frequencies of its QNM oscillations [12, 13], although the relative amplitudes of the modes depend on the specific details of the excitation.

Detection of the characteristic ringdown GW signal of a BH would, therefore, allow a direct test of the no-hair theorem [14], and hence GR, through the comparison of frequencies and decay times of these modes with the predictions of GR for a BH with certain mass and spin. In practice, the detection and discrimination of multiple modes is essential, as it is first necessary to infer the mass and spin of the black hole before checking for consistency between the modes. If any of the modes have some parameter dependence, other than mass and spin, then the mass and spin obtained from these modes will not be consistent with that obtained from the others, and thus the source of emission must not be a Kerr black hole.

In Ref. [14] Dreyer *et al* first developed the formalism

for testing GR with QNM. They also suggested the test of the no-hair theorem through the measurement of more than one mode. Berti *et al*, [15, 16] investigated the accuracy of measurement of individual mode parameters using a Fisher matrix analysis and estimated the resolvability of individual modes in the complete signal as a function of signal-to-noise ratio. They conclude that the presence of a second mode can be inferred as long as the signal-to-noise ratio (SNR) is larger than a critical value, under the assumption that the presence of a ringdown signal has been confirmed and the parameters of the dominant modes are reliably measured. The critical SNR depends on the mass ratio of the progenitor binary but an SNR of 20 should suffice if the mass ratio of the progenitor binary is  $q = m_1/m_2 \gtrsim 2$ . Kamaretsos *et al* showed recently that using black hole ringdown signals that are emitted after a binary merges, it might be possible to recover the mass ratio of the progenitor binary from relative amplitudes of the QNMs [17]. Their signal model, however, is based on non-spinning black hole binaries. Spins might induce systematic effects that could make it difficult to reliably measure the mass ratio of progenitor binary. However, we have to await ringdown models for spinning black hole binaries to assess what might or might not be possible to measure.

Kamaretsos *et al* [17] also proposed different ways of testing GR using QNMs. In particular, they proposed that it is sufficient to use any three of the observed frequencies and decay times for checking the consistency of the ringdown signal with GR. This *minimal set* of parameters could make the test far more effective than trying to resolve the different mode frequencies and decay times. This is one approach we shall follow in this work.

More specifically, in this paper we explore the fea-

sibility of the proposal in Ref. [17] for a limited set of sources and parameter values. Our study is also limited to sources with mass ratio 1:2. We find that for the specific ringdown model that neglects progenitor spins, it is possible to infer the total mass and spin of the black hole and the mass ratio of the progenitor binary from the observed ringdown GW, using a phenomenological mapping from these to the mode parameters. Having established this, we extend our waveform model to include arbitrary deviations from the predicted values of the frequencies and decay times, which can be estimated either along with the physical parameters of the source or on their own, if we assume no relationship between the complex QNM frequencies and the mass and angular momentum of the BH. This gives us two methods of testing GR:

1. Measure the QNM parameters individually and check for consistency between the implied mass and angular momentum from each of the modes.
2. Assume that the GR waveform is broadly correct but allow deviations in the parameters of a subset of the QNMs away from their predicted values and then perform model selection between the GR and non-GR models.

We study both of these techniques in the context of future space- and ground-based detectors, particularly the Einstein Telescope [18, 19] and a rescoped version of the Laser Interferometer Space Antenna called New Gravitational Observatory (NGO).

The rest of the paper is organised as follows: In Section II we define the waveform model and describe the analysis methods used in testing the no-hair theorem. In Section III we will discuss the expected sensitivities of ET and NGO and the distribution of the signal-to-noise ratio of ringdown signals in these detectors. Section IV describes the simulations of the tests of the no-hair theorem using two different methods: (1) consistency of the various parameters characterizing a ringdown signal and (2) Bayesian model selection applied to simulated ringdown signals buried in Gaussian background. Section V contains comparisons of the two methods used in testing GR and our conclusions.

## II. SIGNAL MODEL AND ANALYSIS METHOD

In this Section we will discuss the nature of the ringdown waveform used in this study. The main focus will be to use a superposition of quasi-normal modes containing not only the dominant mode but also the first two sub-dominant ones. Ringdown signals that we study are assumed to be emitted by deformed black holes that form from the merger of compact binaries consisting of *non-spinning* components in quasi-circular orbits. The latter assumption allows us to use a phenomenological waveform model based on numerical relativity simulations; the observed signal is characterised by only three

intrinsic parameters: the mass and spin of the final black hole and the mass ratio of the progenitor binary.

### A. Ringdown model

A perturbed black hole emits a spectrum of modes characterized by three numbers  $(l, m, n)$ . Indices  $l = 2, 3, \dots$ , and  $m = -l, \dots, +l$ , are the well-known spherical harmonic indices, and  $n = 0, 1, 2, \dots$ , is the mode overtone index. Overtones other than the fundamental  $n = 0$  mode are not excited with significant amplitudes and have much shorter damping times [15]. We shall therefore only consider the fundamental mode and drop the index from further discussion.

The two polarisations of the gravitational waveform,  $h_+$  and  $h_\times$ , emitted by a BH of mass  $M$  during its ringdown are described as the sum over the QNMs,

$$h_+(t) = \frac{M}{r} \sum_{l,m>0} A_{l|m|} e^{-t/\tau_{lm}} Y_+^{lm} \cos(\omega_{lm}t - m\phi), \quad (1)$$

$$h_\times(t) = -\frac{M}{r} \sum_{l,m>0} A_{l|m|} e^{-t/\tau_{lm}} Y_\times^{lm} \sin(\omega_{lm}t - m\phi), \quad (2)$$

for  $t \geq 0$  and  $h_+ = h_\times = 0$ , for  $t < 0$ ,  $t = 0$  being the start of the ringdown signal. Here  $r$  is the luminosity distance to the black hole,  $A_{l|m|}(q)$  are the mode amplitudes that depend only on the ratio  $q = m_1/m_2$  ( $m_1 > m_2$ ) of the component masses of the progenitor binary, and  $\tau_{lm}(M, j)$  and  $\omega_{lm}(M, j)$  are the characteristic mode damping times and frequencies. The mode damping times and frequencies depend only the black hole mass  $M$  and its spin  $j$ , but they are difficult to compute analytically. It is necessary to use numerical methods to compute them [11]. Fits to some of the lower order modes can be found in Berti et al [15].  $\iota \in [0, \pi]$  is the angle between the BH spin-axis and the line-of-sight to the observer and  $\phi \in [0, 2\pi]$  is the azimuth angle of the black hole with respect to the observer.  $Y_{+,\times}^{lm}(\iota)$  are the sum of spin  $-2$  weighted spherical harmonics [16],

$$Y_+^{lm}(\iota) \equiv -{}_2Y^{lm}(\iota, 0) + (-1)^l {}_2Y^{l-m}(\iota, 0), \quad (3)$$

$$Y_\times^{lm}(\iota) \equiv -{}_2Y^{lm}(\iota, 0) - (-1)^l {}_2Y^{l-m}(\iota, 0). \quad (4)$$

Although the waveform in Eqs. (1) and (2) contains a summation of modes over all values of  $l$  and  $m$ , the relative amplitudes of the higher order modes are significantly less than those of the lower, so we restrict the sum to the most significant modes. The waveform considered for this analysis is a superposition of the  $n = 0$ ,  $l = 2$ ,  $m = 1$  and  $n = 0$ ,  $l = m = \{2, 3, 4\}$  modes (which will hereafter be referred to as the 21, 22, 33 and 44 modes, respectively) with the 22 mode being dominant.

The relative dominance of the higher order modes is dependent on the specific excitation that occurred (through

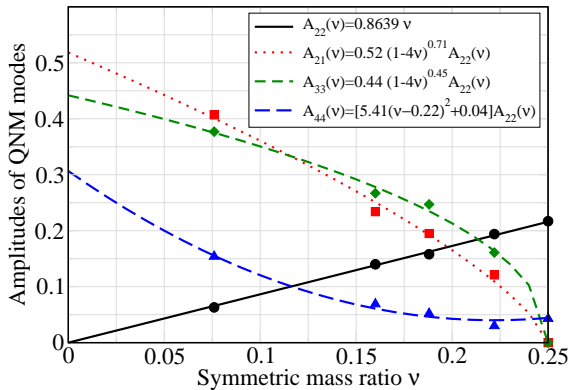


FIG. 1: Fits to the amplitudes of modes excited in the process of a binary black hole merger as a function of the symmetric mass ratio of the progenitor binary.

$A_{lm}$ ) and the position of the observer (through  $Y_{lm}$ ). This depends on both the mass ratio  $q = m_1/m_2 \geq 1$  of the compact binary components prior to merger, and the inclination angle  $\iota$ . We used a phenomenological model based on fits to a set of numerical simulations to describe the mode amplitudes. We used the data in Kamaretsos *et al* [17], but instead of using the mass ratio  $q$  we used the symmetric mass ratio  $\nu = m_1 m_2 / (m_1 + m_2)^2 = q / (1 + q)^2$  to derive new physically motivated fits. The 22 mode is expected to grow linearly with the symmetric mass ratio as noted in Refs. [20, 21]. Modes with odd  $l$  or  $m$  are not expected to be excited when the progenitor binary is of equal mass and so we expect their behaviour close to  $\nu = 1/4$  to be some power of  $(1 - 4\nu)$ . These considerations led us to the following forms of the various amplitudes:

$$A_{22}(\nu) = 0.864\nu, \quad (5)$$

$$A_{21}(\nu) = 0.52(1 - 4\nu)^{0.71} A_{22}(\nu), \quad (6)$$

$$A_{33}(\nu) = 0.44(1 - 4\nu)^{0.45} A_{22}(\nu), \quad (7)$$

$$A_{44}(\nu) = [5.4(\nu - 0.22)^2 + 0.04] A_{22}(\nu). \quad (8)$$

Figure 1 plots the above fits together with the amplitudes of the various modes derived from numerical simulations. The current data seems to indicate that  $\hat{A}_{44} \equiv A_{44}(\nu)/A_{22}(\nu)$  has a minimum at  $\nu = 0.22$ . However, the amplitude of the 44 mode derived from numerical simulations is not very reliable and so this might be just an artifact of bad data. More accurate simulations are needed to validate this result.

To complete the signal model we have to specify the damping constants  $\tau_{\ell m}$ . Instead of damping times  $\tau_{\ell m}$  it is customary to use *quality factors*  $Q_{\ell m}$  defined by  $Q_{\ell m} = \omega_{\ell m} \tau_{\ell m} / 2$ . Berti *et al* [15] provide a simple fitting formula to many mode frequencies and quality factors of

the form:

$$M\omega = f_1 + f_2(1 - j)^{f_3} \quad (9)$$

$$Q = q_1 + q_2(1 - j)^{f_3} \quad (10)$$

where  $f_1, f_2, f_3, q_1, q_2$  and  $q_3$  are fitting constants. For the modes considered in this paper Table I lists the fitting constants.

$(l, m)$	$f_1$	$f_2$	$f_3$	$q_1$	$q_2$	$q_3$
(2, 1)	0.6000	-0.2339	0.4175	-0.3000	2.3561	-0.2277
(2, 2)	1.5251	-1.1568	0.1292	0.7000	1.4187	-0.4990
(3, 3)	1.8956	-1.3043	0.1818	0.9000	2.3430	-0.4810
(4, 4)	2.3000	-1.5056	0.2244	1.1929	3.1191	-0.4825

TABLE I: The fitting constants in Eqns. (9) and (10), for the 21, 22, 33 and 44 modes, for the dominant  $n = 0$  overtone [15].

The gravitational-wave strain observed by a detector due to the excitation of QNM can be expressed as

$$h = F_+ h_+ + F_\times h_\times \quad (11)$$

where  $F_+$  and  $F_\times$  are the detector antenna pattern functions, which depend on the position  $(\theta, \varphi)$  of the black hole relative to the detector and polarisation angle  $\psi$  of the radiation (see Ref. [17] for details). The measured strain, therefore, depends on the following 9 parameters:

$$\vec{\theta} = \{M, \nu, r, \theta, \varphi, \psi, \iota, \phi, t_0\}, \quad (12)$$

which includes the epoch  $t_0$  when the signal arrives at our detector<sup>1</sup>.

Figure 2, left panel, shows the response of a signal containing all four modes considered in this work as well as the phase evolution of each of modes 21, 22, 33 and 44 for a  $5 \times 10^6 M_\odot$  black hole at a distance of 1 Gpc, assumed to be formed from a binary of mass ratio  $q = 2$ . The black hole is assumed to be overhead with respect to the detector, the orbital plane making an angle of  $\iota = \pi/3$  radians — a sub-optimal orientation but one for which the sub-dominant modes will have a nonzero amplitude. The polarization and azimuth angles are randomly chosen to be  $\psi = 2.67$  radians and  $\phi = 2.31$  radians.

The overall amplitude is very nearly the same as that of the 22 mode. The amplitude of the 33 mode, which is the second most dominant after 22, is about a third of the 22 mode, followed by the 21 mode, which has a slightly smaller amplitude. The 44 mode, whose amplitude is about 12% of the 22 mode, has negligible effect on the overall signal. Although 21 and 33 are of roughly the same amplitude, the energy in 33 mode, whose frequency

<sup>1</sup> Note that Eqs.(1) and (2) are written assuming  $t_0 = 0$ . A nonzero value of  $t_0$  can be trivially included in the signal model by writing  $t$  as  $t - t_0$  and assuming  $h_{+, \times}(t) = 0$  for  $t < t_0$ .

is roughly twice that of 21, will be significantly larger as we will see in Sec. III, while discussing the relative signal-to-noise ratios of the different modes. The interference between the different modes causes features that become apparent in the spectrum of the modes shown in the left hand panel of Figure 2, which we will discuss further in Sec. III.

### B. A generalised model for the QNM

In order to test GR, we extended the waveform model so that the frequencies and decay times of the modes were allowed to be dependent not only on  $M$  and  $j$ , but also other dimensionless parameters. More specifically, we considered that frequencies  $\omega_{lm}$  depended on three parameters ( $M, j, \Delta\hat{\omega}_{lm}$ ) and damping times  $\tau_{lm}$  also depended on three parameters ( $M, j, \Delta\hat{\tau}_{lm}$ ). Furthermore, we assumed that the dimensionless parameters  $\Delta\hat{\omega}_{lm}$  and  $\Delta\hat{\tau}_{lm}$  were independent for each mode. Following Li et al [22], in this generalised model, the frequencies  $\omega_{lm,\text{nonGR}}$  and decay times  $\tau_{lm,\text{nonGR}}$  were expressed as

$$\omega_{lm,\text{nonGR}} = \omega_{lm,\text{GR}} (1 + \Delta\hat{\omega}_{lm}) \quad (13)$$

$$\tau_{lm,\text{nonGR}} = \tau_{lm,\text{GR}} (1 + \Delta\hat{\tau}_{lm}) \quad (14)$$

where  $\omega_{lm,\text{GR}}$  and  $\tau_{lm,\text{GR}}$  are the frequencies and decay times of modes as in GR. The signal produced by the GR hypothesis is a special case of the generalised model, in which  $\Delta\hat{\omega}_{lm} = \Delta\hat{\tau}_{lm} = 0$  for all  $l, m$ .

### C. Bayesian analysis

Having described the waveform model and its parameters (contained in a parameter vector  $\vec{\theta}$ ), we will now describe how these parameters are estimated from data containing a ringdown signal. We assume that the data from the gravitational wave detector in the frequency domain  $\tilde{d}$  contains both the ringdown signal  $\tilde{h}(f; \vec{\theta})$  and some additive Gaussian noise with known power spectrum  $S_h(f)$ . Thus, the data  $\tilde{d}$  is assumed to be  $\tilde{d}_i = \tilde{h}(f_i; \vec{\theta}) + \tilde{n}_i$ , where  $i$  is the index of the frequency bin. The noise power spectra used for ET and NGO are given in Section III A. As we perform our analysis in the frequency domain, we use the Fourier transformed signal model  $\tilde{h}(f) = \int_0^\infty h(t)e^{-2\pi if t} dt$  computed with the FFTW package.

Our goal is to compute the posterior probability distribution (PDF) (see, for instance, Ref. [23]), of the parameters  $p(\vec{\theta}|d, \mathcal{H})$ ,

$$p(\vec{\theta}|d, \mathcal{H}) = \frac{p(d|\vec{\theta}, \mathcal{H})p(\vec{\theta}|\mathcal{H})}{p(d|\mathcal{H})}, \quad (15)$$

where  $p(d|\mathcal{H})$  is the evidence, or marginal likelihood, of the model

$$p(d|\mathcal{H}) = \int_{\Theta} p(\vec{\theta}|\mathcal{H})p(d|\vec{\theta}, \mathcal{H})d\vec{\theta}, \quad (16)$$

$\mathcal{H}$ ,  $p(\vec{\theta}|\mathcal{H})$  is the prior distribution of the parameters given the signal model and  $p(d|\vec{\theta}, \mathcal{H})$  is the likelihood of the data for a particular set of parameters  $\vec{\theta}$ :

$$p(d|\vec{\theta}, \mathcal{H}) \propto \exp\left(-2 \sum \frac{|\tilde{d}_i - \tilde{h}(f_i; \vec{\theta})|^2}{S_h(f_i)}\right). \quad (17)$$

Posterior distributions for particular parameters of interest, e.g. the  $\Delta\hat{\omega}_{lm}$  and  $\Delta\hat{\tau}_{lm}$ , are computed by marginalising the PDF over all other parameters. We also compute the Bayes factor  $B_{i,j}$  between various hypotheses,  $B_{i,j} = p(d|i)/p(d|j)$ , which is the evidence ratio between hypotheses  $i$  and  $j$ . Due to the large range of this quantity we will always use the natural logarithm of this,  $\log B_{i,j}$ , in section IV C.

To compute the PDFs and evidence we use the `inspnest` implementation of the nested sampling algorithm, described in [23], modified to use the ringdown signal model, which is available as part of the LSC Algorithm Library [24]. The end product of the analysis is the model evidence and a set of samples from the posterior PDF that are histogrammed to produce the figures below.

## III. VISIBILITY OF THE QNM SIGNALS

In this Section we will explore the visibility of quasi normal mode signals. We will begin with the expected sensitivities of ET and NGO and then go on to explore the visibility of the signal in these two detectors. The signal-to-noise ratio (SNR) of a ringdown signal depends quite critically on a number of intrinsic and extrinsic parameters of the source. We will vary most of these parameters to obtain a distribution of the SNR.

### A. Sensitivity curves

In this paper, the ET and NGO detectors are considered. For simulations concerning ET, the power spectral density corresponding to the ET-B sensitivity curve is considered, described by  $S_h(f) = 10^{-50}h_n(f)^2 \text{Hz}^{-1}$ , where  $h_n(f)$  is given by

$$h_n(f) = 2.39 \times 10^{-27}x^{-15.64} + 0.349x^{-2.145} + 1.76x^{-0.12} + 0.409x^{1.10},$$

and  $x = f/100\text{Hz}$ . For NGO, the sensitivity curve associated with the  $L = 1 \times 10^9$  m arm, 4-link mission studied in Ref. [25], which corresponds to a power spectral density given by

$$S_h(f) = \frac{10}{3L^2} \left(1 + \left[\frac{2Lf}{0.41c}\right]^2\right) (4S_{acc} + S_0), \quad (18)$$

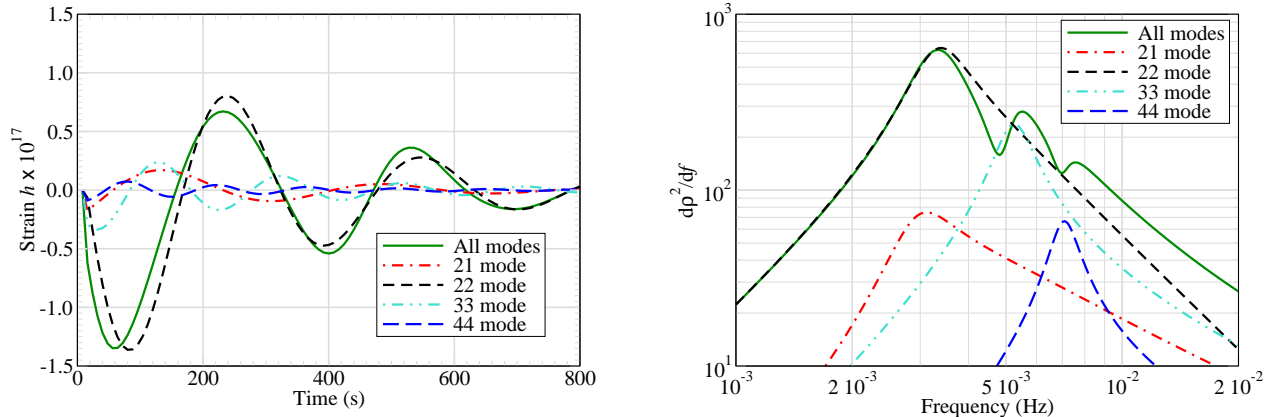


FIG. 2: *Left*: Strain amplitude of a quasi-normal mode signal from a black hole that forms from the merger of a binary of (observed) total mass  $5 \times 10^6 M_\odot$  and mass ratio  $q = 2$  at 1 Gpc. We have plotted the first four dominant modes, 21, 22, 33 and 44 together with their superposition. *Right*: The signal-to-noise ratio integrand of the same signal  $d\rho^2/df = |H(f)|^2/S_h(f)$ , where  $S_h(f)$  is taken to be that of NGO. The presence of the 33 and 44 mode can be clearly seen in the overall spectrum, 21, however, is buried under 22.

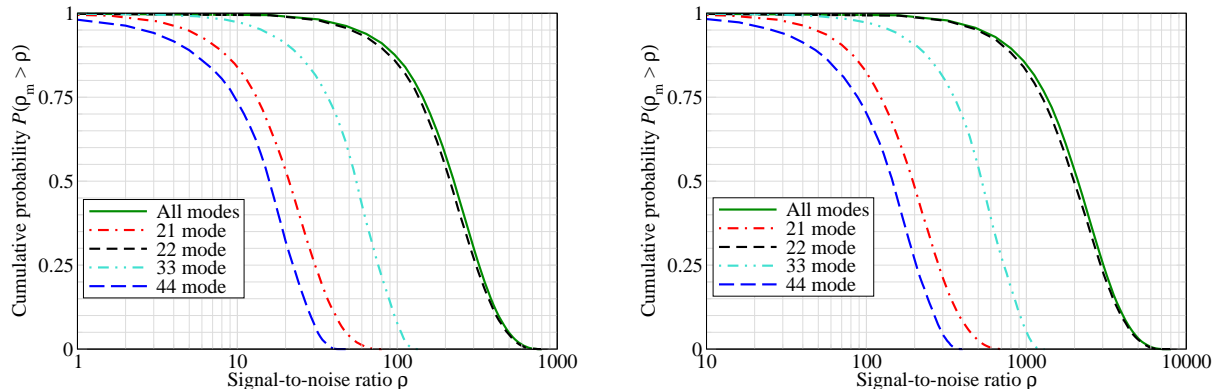


FIG. 3: Distribution of the signal-to-noise ratios in different quasi-normal modes (21, 22, 33 and 44) for sources located at random positions on the sky, with random inclination and polarisation angles. The left plot is for QNM resulting from the merger of a 500 solar mass binary observed in ET and the right plot is for a 5 million solar mass binary observed in NGO. In both cases the mass ratio of the binary is assumed to be  $q = 2$  and the source is assumed to be at 1 Gpc.

where,  $S_0 = 1.153 \times 10^{-22} \text{ m}^2 \text{ Hz}^{-1}$  and

$$S_{acc} = 1.37 \times 10^{-32} \left( 1 + \frac{10^{-4} \text{ Hz}}{f} \right) \left( \frac{2\pi f}{1 \text{ Hz}} \right)^{-4} \text{ m}^2 \text{ Hz}^{-1}. \quad (19)$$

## B. Visibility of ringdown signals

An important requirement for tests of the no-hair theorem is good visibility of the signal in our detector: larger the signal-to-noise ratio (SNR), greater would be the

power of the test. The SNR depends both on the intrinsic parameters of the black hole, its mass and spin angular momentum, as well as its extrinsic parameters, its distance and various angles describing the orientation of its spin axis, its location on the sky and the polarisation of the radiation. In this Section we will look at the distribution of the SNR in ET and eLISA/NGO.

The SNR of a ringdown signal observed using matched filtering is given by

$$\rho^2 = 4 \int_{f_{\text{low}}}^{f_{\text{high}}} \frac{|H(f)|^2}{S_h(f)} df, \quad (20)$$

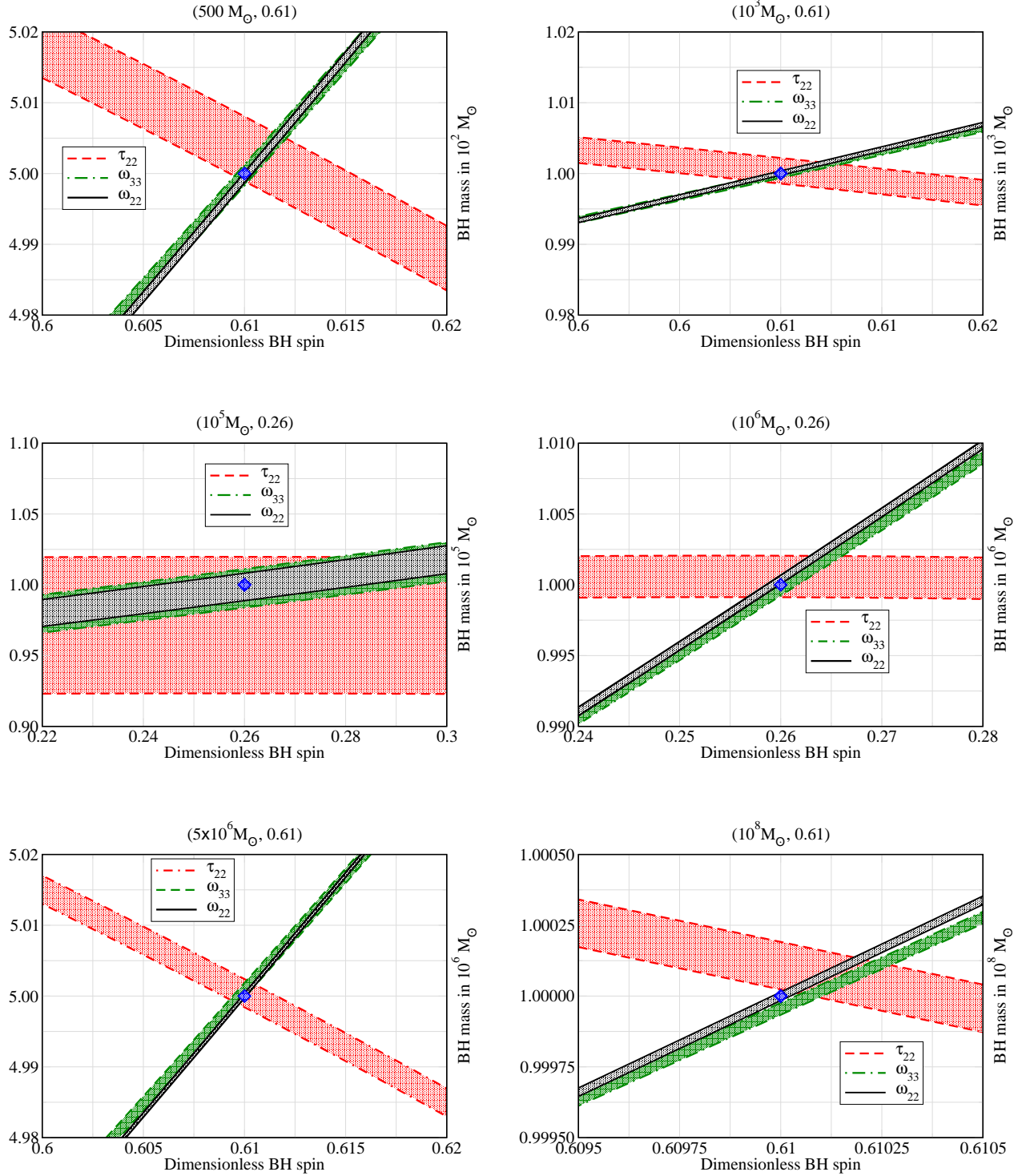


FIG. 4: Projections in the  $(M, j)$ -plane of the 90% confidence limits on  $\omega_{22}$ ,  $\tau_{22}$  and  $\omega_{33}$  (blue, blue dotted and red lines respectively) for injections of signals consistent with GR for  $M = 500 M_{\odot}$  (top-left at 125 Mpc; SNR = 2888),  $M = 1000 M_{\odot}$ , (top-right at 225 Mpc; SNR = 2423);  $M = 10^5 M_{\odot}$  (middle-left at 125 Mpc; SNR = 63),  $M = 10^6 M_{\odot}$  (middle-right at 125 Mpc; SNR = 1756),  $M = 5 \times 10^6 M_{\odot}$  (bottom-left at 1 Gpc; SNR = 6377) and  $M = 10^8 M_{\odot}$  (bottom-right at 1 Gpc; SNR = 115154). The injected value is denoted in each case by a diamond.

where  $S_h(f)$  is the detector noise power spectral density and  $H(f)$  is the Fourier transform of the signal in Eq. (11). The limits on the integrand can, in principle, be from 0 to  $\infty$ . However, in order to prevent the “junk” radiation that occurs in the Fourier transform due to abrupt cutoff of the time-domain signal from corrupting the SNR we choose finite values for both them. More concretely, we choose  $f_{\text{low}}$  to be half of the smallest signal frequency (which in our case is that corresponding to the 21 mode) and  $f_{\text{high}}$  to be twice the highest signal frequency (which in our case is that corresponding to the 44 mode).

$\rho$  is the SNR of the signal containing all the modes considered in this paper. To test the no-hair theorem it is essential that the SNRs of the sub-dominant modes (21, 33, 44) are comparable to the dominant 22 mode. To assess their importance, we shall also separately consider the SNR  $\rho_{\ell m}$  of each mode:

$$\rho_{\ell m}^2 = 4 \int_{f_{\text{low}}}^{f_{\text{high}}} \frac{|H_{\ell m}(f)|^2}{S_h(f)} df, \quad (21)$$

where  $H_{\ell m}$  is the Fourier transform of the signal in Eq. (11) but with  $h_+$  and  $h_\times$  containing only the relevant mode. We will compare the distribution of  $\rho_{\ell m}$  for  $\ell m = 21, 22, 33$  and 44 modes but it should be kept in mind that  $\rho^2$  is not the sum over different  $\rho_{\ell m}^2$ . Even so, the relative strengths of different modes gives us an indication of how good we can expect our tests of the no-hair theorem to be.

Figure 2, right panel, plots the SNR integrand  $d\rho^2/df$  of the various modes. The overall signal gets most of its contribution from the 22 mode but other modes significantly alter the phasing of the signal (left panel) and its spectrum. The overall signal has bumps caused by the 33 and 44 modes but the 21 mode, whose frequency is close to that of 22, has little effect on the overall amplitude or the phasing of the waves. Note that the spectrum of 33 is far larger than the 21 mode although they are of similar amplitude.

Figure 2 gives a qualitative understanding that the subdominant modes have significant effect on the phasing and spectrum of the signal. But we need to evaluate the distribution of the SNR to better gauge the relative importance of the different modes. The response of our detectors to a ringdown signal depends on a total of nine parameters as enumerated in Eq. (12). To compute the distribution of the SNR, however, we don’t need to vary all nine parameters. We know that the SNR depends inversely on the luminosity distance  $r$  of the source and so this can be fixed to any value we wish and we take it to be  $r = 1$  Gpc. The distribution does not depend on the epoch of the signal  $t_0$  nor on the phase  $\phi$ . We should study the distribution as a function of  $M$  and  $\nu$  while varying the remaining four parameters. However, since our goal is to explore the test of the no-hair theorem for a small sample of signals with high SNR we will restrict ourselves to only a couple of sources. We will consider a BH that results from the merger of a  $500 M_\odot$  binary in

the case of ET and a  $5 \times 10^6 M_\odot$  binary in the case of NGO. In both cases we take the symmetric mass ratio to be  $q = 2$  or  $\nu = 2/9$ .

The cumulative distribution of the SNR is shown in Figure 3. We see that there is a 25% chance that the SNR will be greater than 300 in ET and 3000 in NGO. The corresponding SNR in the 33 mode is 90 and 900 for ET and NGO, respectively. Even the least dominant 44 mode has SNRs of 20 and 200. The SNRs drop off as inverse distance and at redshifts  $z \sim 1-3$ , from within which we can expect the event rate of massive black holes to be in excess of several per year, the SNRs will be still large enough that NGO should be able to carry out meaningful tests of GR for a large fraction of sources detected. Only very rare closeby events will allow such tests in the case of ET.

#### IV. TESTS OF THE NO-HAIR THEOREM

In this Section we will explore the ability of ET and NGO to test the no-hair theorem if they were to detect a ringdown signal from a black hole that resulted from the coalescence of a binary. We will begin with a summary of the parameters used in our simulations followed by a description of the two different approaches that were used to test the no-hair theorem. The first method uses consistency of the various mode frequencies and damping constants with GR predictions and the second method is a Bayesian model selection approach that addresses which of a class of different models best describes the underlying signal. We find that the latter approach is far more powerful in testing the no-hair theorem.

The model selection approach followed in this paper is computationally pretty expensive. We have therefore selected a small sample of signals (two in ET and four in NGO) to assess how well future detectors are able to test the no-hair theorem. The SNR study from the foregoing Section can be used to conclude how effective such tests are for a random signal detected in our instruments.

##### A. Choice of injection parameters

The GW signal emitted from the QNM of a black hole ringdown as observed in a detector depends on the mass and spin of the final BH, the mass ratio of the progenitor binary and other extrinsic parameters that describe the orientation of the black hole, its distance from the detector and its position on the sky. For the different sensitivity bands of ET and NGO we chose the following range of source parameters. For ET, black holes of observed mass  $500 M_\odot$  and  $1000 M_\odot$  at luminosity distances,  $D_L$ , from 125 Mpc and 225 Mpc respectively, out to 6.63 Gpc (corresponding to redshift  $z \simeq 1$  [26]), were considered. For NGO, black holes of observed mass  $5 \times 10^6$  and  $10^8 M_\odot$  at  $D_L = 1 - 59$  Gpc (with the upper limit corresponding to a redshift  $z \simeq 6$ ), and black holes of observed mass  $10^5$

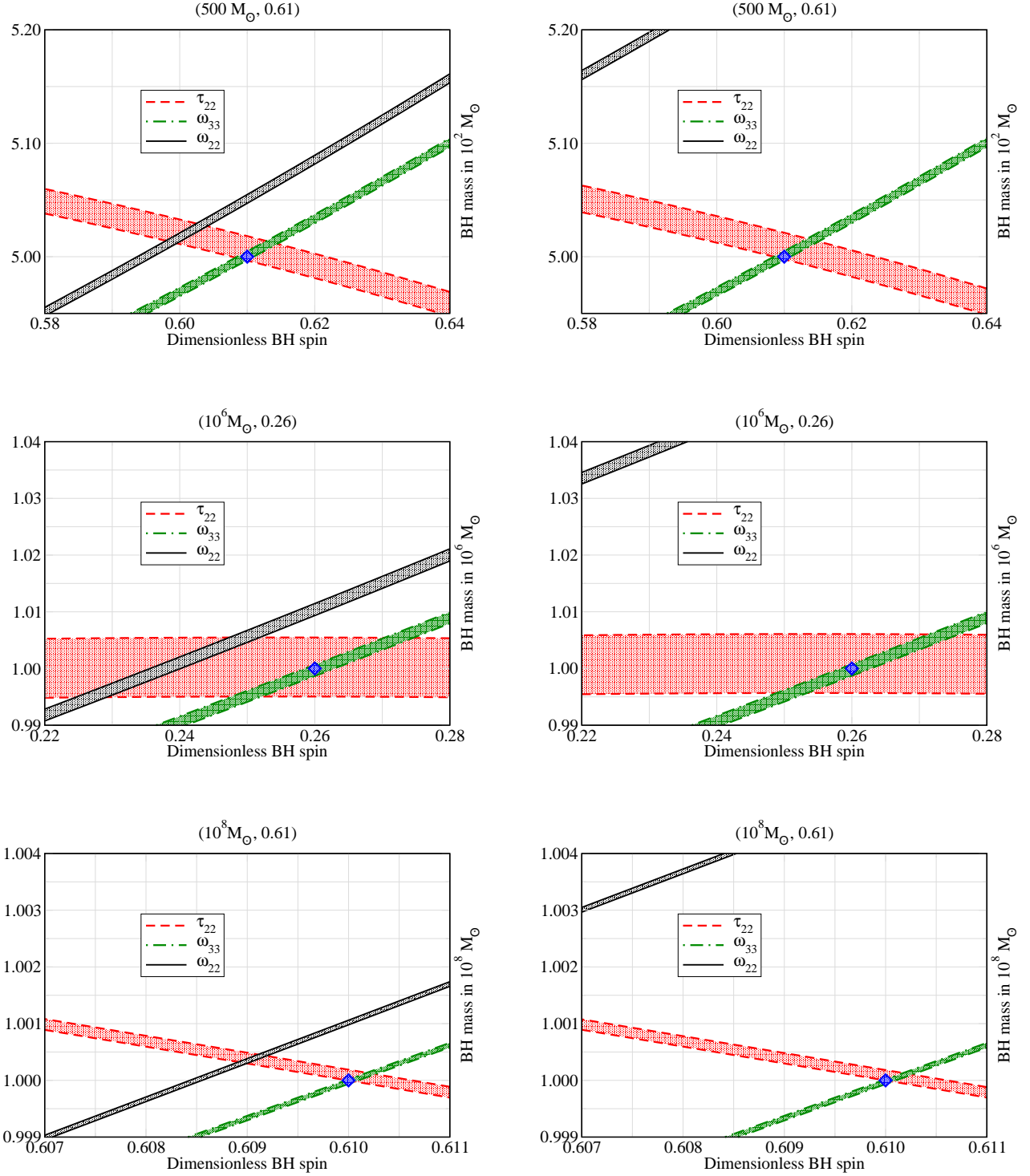


FIG. 5: Projections in the  $(M, j)$ -plane of the 90% confidence limits on  $\omega_{22}$ ,  $\tau_{22}$  and  $\omega_{33}$  (blue, blue dotted and red lines, respectively) for non-GR injections of  $M = 500 M_{\odot}$  (top at 125 Mpc; with  $\Delta\hat{\omega}_{22} = -0.01$ , SNR = 2 867 (left) and  $\Delta\hat{\omega}_{22} = -0.05$ , SNR = 2 779 (right)),  $M = 10^6 M_{\odot}$  (middle at 125 Mpc; with  $\Delta\hat{\omega}_{22} = -0.01$ , SNR = 1 753 (left) and  $\Delta\hat{\omega}_{22} = -0.05$ , SNR = 1 735 (right)) and  $M = 10^8 M_{\odot}$  (bottom at 1 Gpc; with  $\Delta\hat{\omega}_{22} = -0.001$ , SNR = 115 130 (left) and  $\Delta\hat{\omega}_{22} = -0.005$ , SNR = 115 031 (right)). The injected value is denoted in each case by a diamond.



and  $10^6 M_\odot$  at  $D_L = 125 \text{ Mpc} - 6.63 \text{ Gpc}$ , were considered. In both cases, the source position  $(\alpha, \delta)$  was set to be directly above the detector at the time of observation.

For all systems, the inclination and polarisation angles  $(\iota, \psi)$  were set to be  $(\frac{\pi}{3}, \frac{\pi}{3})$  and the azimuth  $\phi$  was taken to be zero. For the first four systems described, the mass ratio  $q$  of the binary system prior to merger and the spin  $j$  of the black hole after merger were set to  $q = 2$  and  $j = 0.61$ , respectively. For the final two systems outlined, however,  $q = 10$  and  $j = 0.26$ , to represent a more typical NGO binary system. For the sake of using the phenomenological fit in table I the binary components were assumed to be non-spinning. It is important to note, especially for NGO, that the observed mass of the system is redshifted to be greater than the intrinsic mass of the system by a factor of  $(1+z)$ . Here we report this observed, redshifted mass for injections and recovery.

For injections consistent with GR, parameters  $\Delta\hat{\omega}_{lm} = \Delta\hat{\tau}_{lm} = 0$ , whereas for non-GR signals, either  $\Delta\hat{\omega}_{22}$  or  $\Delta\hat{\tau}_{22}$  was varied in the range  $-0.01 \dots -0.1$ , with all other  $\Delta\hat{\omega}_{lm} = \Delta\hat{\tau}_{lm} = 0$ .

## B. Constraining QNM parameters

Having established the parameters of our test sources, we now move on to consider the two tests of GR. The first method broadly follows the outline of Ref. [17] to estimate the parameters of each QNM in the ringdown signal. By choosing two of the measurements one can infer the true mass and spin of the black hole by excluding regions in the  $M, j$  plane which are inconsistent with the measured parameters. The third measurement is then used to confirm the consistency of the inference. In the case of GR the allowed area will intersect both the previous areas as in Figure 4. Alternatively, if the signal is inconsistent with GR the intersections of the confidence regions will not agree, as in Figure 5.

In order to compute the constraints, we find the upper and lower 90% probability interval of the marginal posterior probability distribution of the parameters  $\Delta\hat{\omega}_{lm}$  and  $\Delta\hat{\tau}_{lm}$ . In each case the injected values of these parameters were set to 0, corresponding to the GR waveform. The priors for  $\Delta\hat{\tau}_{lm}$  and  $\Delta\hat{\omega}_{lm}$  were all uniform in the interval  $[-1.0, 0.3]$  for all analyses, and the  $M, j$  and  $q$  parameters were set to their injected values. As we are estimating the mode parameters directly, through  $\Delta\hat{\omega}_{lm}$  and  $\Delta\hat{\tau}_{lm}$ , the values of  $M$  and  $j$  parameters do not play any role in the results other than to set the centre of the prior range. The reason for the asymmetric choice of interval is that by allowing  $\Delta\hat{\omega}_{22}$  to be greater than 0.3, the frequencies of the 22 and 33 modes collide, leading to strong correlations between the parameters of these modes upon recovery and confusion between the modes. Note that we allow the frequency of the 33 mode to vary downward into the band of the 22 mode, but this does not result in difficulties as the 22 mode is already within

this band, making its identification easier. In all searches, the luminosity distance of the source and orientation angles are assumed known and fixed to the aforementioned values.

We chose the  $\Delta\hat{\omega}_{22}$ ,  $\Delta\hat{\tau}_{22}$  and  $\Delta\hat{\omega}_{33}$  parameters to perform our consistency test as these are the three recovered parameters with the greatest precision for the signals we considered, and will therefore give the most stringent test.

We first injected signals using the GR waveform and performed parameter estimation on the three test parameters. The 90% probability limits on  $\omega_{lm}$  and  $\tau_{lm}$  were projected in the  $(M, j)$ -plane to show visually the consistency test between the three modes, and that they agree at the injected value  $(M, j)$  within the measurement accuracy. Figure 4 shows that for each system, the projections of  $\omega_{lm}$  and  $\tau_{lm}$  coincide at the same position, and the region of coincidence encloses the injected value of the mass and spin of the system, as expected.

To contrast, in Figure 5 we show the corresponding plots where the injection is performed with deviations from GR of  $\Delta\hat{\omega}_{22}$  of  $-0.01$  and  $-0.05$  for both ET and the  $10^6 M_\odot$  NGO system, whilst for the  $10^8 M_\odot$  NGO system, deviations of  $-0.001$  and  $-0.005$  were considered (all other parameters are taken to be the same).

This demonstrates the feasibility of the method for testing the no-hair theorem using consistency of the modes, when the signal is strong and the modes are clearly distinguishable. Of course, we may not be fortunate enough to observe BH ringdowns from such nearby sources, in which case we expect the power of the method to diminish.

To investigate the accuracy to which the mode parameters are resolvable we performed a set of injections at luminosity distances spanning the entire distance range quoted in Section IV A, and estimated the  $\Delta\hat{\omega}_{22}$ ,  $\Delta\hat{\omega}_{33}$  and  $\Delta\hat{\tau}_{22}$  parameters. For each black hole system considered, the width of the 90% confidence intervals for the extracted values of  $\Delta\hat{\omega}_{lm}$  and  $\Delta\hat{\tau}_{lm}$  were plotted against luminosity distance in Figure 6, for injections with GR waveforms. Our results are in agreement with similar studies carried out in Ref. [27]. From Fig. 6, it can be seen that the width of the 90% confidence intervals for the values of  $\Delta\hat{\omega}_{22,33}$  and  $\Delta\hat{\tau}_{22}$  increases with distance, as expected.  $\Delta\hat{\omega}_{33}$  is extracted with considerably less accuracy than  $\Delta\hat{\omega}_{22}$ , because for a black hole system with  $q = 2$ , as considered here, the 33 mode is significantly less excited than the dominant 22 mode, and thus the 33 mode has a much lower SNR, resulting in poorer resolution. By the same token,  $\Delta\hat{\tau}_{22}$  is extracted with considerably less accuracy than both  $\Delta\hat{\omega}_{22,33}$ , as there is less extractable information from the mode decay times as opposed to the mode frequencies. In general, however, the relative weights and SNRs of each mode depends on the source parameters including orientation, and the noise curve of the detector.

We also see that ET can resolve  $\Delta\hat{\omega}_{22}$  with errors of less than 1% at  $D_L = 4 \text{ Gpc}$  for the systems considered,

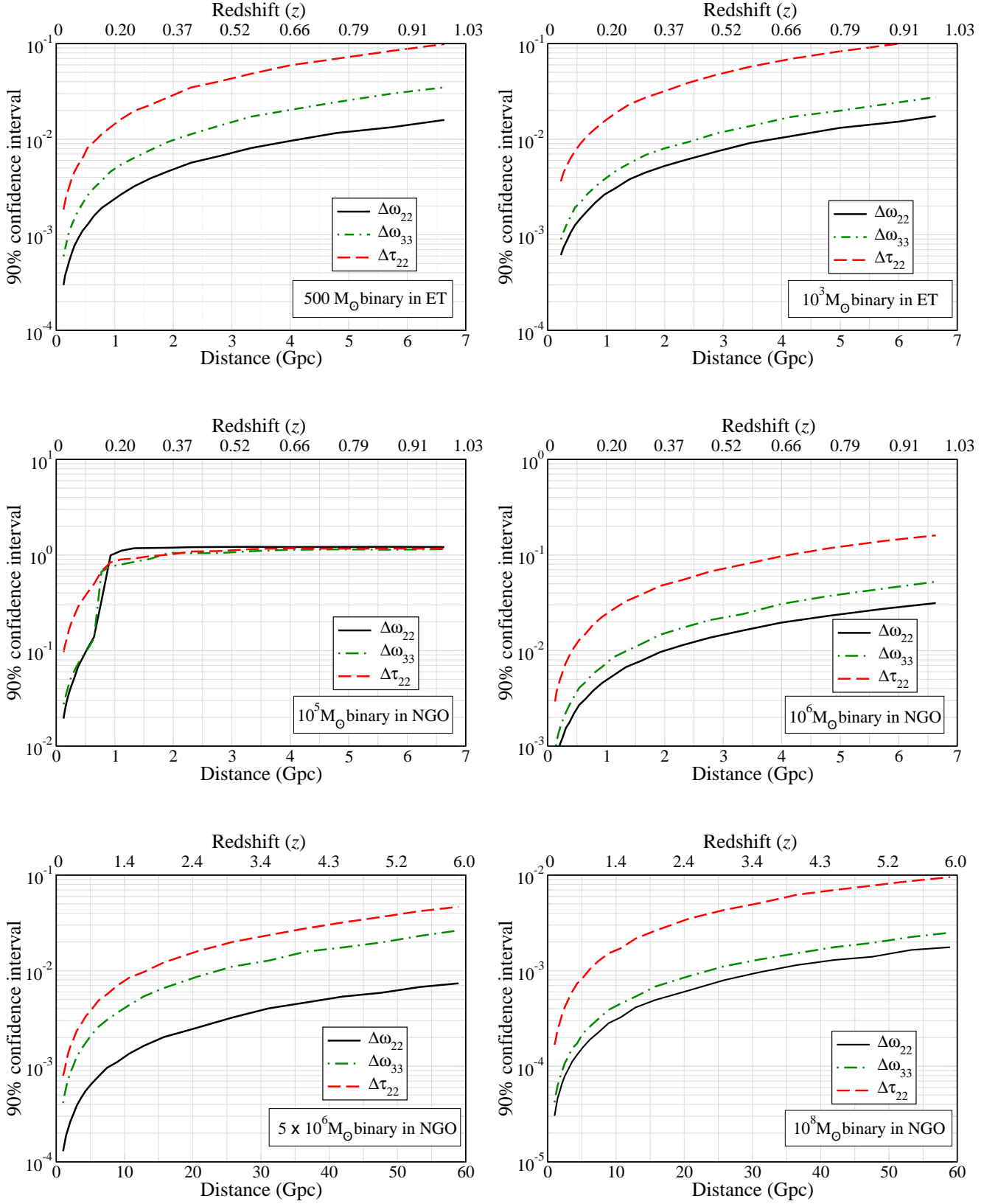


FIG. 6: Width of the 90% confidence intervals for  $\Delta\hat{\omega}_{22}$ ,  $\Delta\hat{\omega}_{33}$  and  $\Delta\hat{\tau}_{22}$  (blue, red and blue dotted lines respectively) against luminosity distance for injections of 500 (top-left), 1000 (top-right),  $10^5$  (middle-left),  $10^6$  (middle-right),  $5 \times 10^6$  (bottom-left) and  $10^8 M_{\odot}$  (bottom-right) for ET (top) and NGO (middle and bottom) simulations. The limiting values in the  $10^5 M_{\odot}$  plot are due to the posteriors expanding to fill the prior distributions when they are no longer resolvable.

in addition to resolving  $\Delta\hat{\omega}_{22,33}$  and  $\Delta\hat{\tau}_{22}$  with errors of 1.5%, 2.5% and 10% for a black hole of  $500 M_\odot$  at  $D_L = 6.63$  Gpc.

NGO can resolve  $\Delta\hat{\omega}_{22}$  to  $\sim 0.6\%$  accuracy at  $D_L = 59$  Gpc ( $z = 6$ ) for both  $5 \times 10^6 M_\odot$  and  $10^8 M_\odot$  systems, showing good results across the range of masses detectable.  $\Delta\hat{\tau}_{22}$  ( $\Delta\hat{\omega}_{33}$ ) can be resolved to  $\sim 3.5\%$  (1.5%) and  $\sim 1\%$  (0.15%) accuracy for  $5 \times 10^6 M_\odot$  and  $10^8 M_\odot$  systems respectively, at this distance. This trend is mirrored for the  $10^6 M_\odot$  system, with NGO able to resolve  $\Delta\hat{\omega}_{22}$  to  $\sim 2\%$  accuracy at  $D_L = 6.63$  Gpc ( $z = 1$ ), and  $\Delta\hat{\tau}_{22}$  ( $\Delta\hat{\omega}_{33}$ ) to 10.5% (5%) at this distance. For the  $10^5 M_\odot$  system however, resolution of  $\Delta\hat{\omega}_{22}$  is poor even at distances of  $D_L = 1$  Gpc, suggesting that it would not be possible to conduct these discriminatory tests using such systems, as they are not expected to exist at distances closer than 1 Gpc.

The method outlined above to test the accuracy with which we can extract the three QNM parameters was applied to the case of non-GR signals ( $\Delta\hat{\omega}_{lm}$  or  $\Delta\hat{\tau}_{lm}$  set to some value within the range quoted in Section IV A, with all other  $\Delta\hat{\omega}_{lm} = \Delta\hat{\tau}_{lm} = 0$ ) from systems of  $M = 500 M_\odot$  and  $10^8 M_\odot$  in ET and NGO. The QNM corresponding to these systems lie closest to the most sensitive frequency regions of the corresponding detectors, so this test is an optimistic case. Also, the distances used were from the lower end of the range quoted in Section IV A. For each non-GR injection, the 90% probability limits on the values of  $\Delta\hat{\omega}_{22}$ ,  $\Delta\hat{\omega}_{33}$  and  $\Delta\hat{\tau}_{22}$  were extracted and used to project the corresponding confidence limits on  $\omega_{lm}$  and  $\tau_{lm}$  in the  $(M, j)$ -plane.

Figure 5 shows that even for deviations from GR of as small as 1% (corresponding to  $\Delta\hat{\omega}_{22} = -0.01$ ) for ET and the  $10^6 M_\odot$  NGO system, and as small as 0.1% (corresponding to  $\Delta\hat{\omega}_{22} = -0.001$ ) for the  $10^8 M_\odot$  NGO system, the projection of  $\omega_{22}$  does not intersect consistently with the projections of  $\tau_{22}$  and  $\omega_{33}$ , which were unchanged from their GR predicted values. When an additional parameter dependence is introduced for one mode parameter, the mass and spin derived from this modified parameter will not be consistent with the mass and spin derived from the other unchanged parameters. For a deviation of 5% for ET and the  $10^6 M_\odot$  NGO system, and 0.5% for the  $10^8 M_\odot$  NGO system, the projection of  $\omega_{22}$  does not even touch the projections of  $\tau_{22}$  and  $\omega_{33}$ , let alone intersect at the correct value. This shows that in extracting the individual mode parameters from a QNM signal and projecting them in the  $(M, j)$ -plane, it is possible to determine if one, or many, of the mode parameters are not consistent with GR and have some parameter dependence other than on the mass and spin.

### C. Discriminating between models

Although we have demonstrated the possibility of performing a consistency test between the QNM parameters by plotting them on the  $(M, j)$  plane, this method does

not provide a quantitative measure of the consistency as such. In this section we seek to provide such a quantification by performing model selection on two competing models: the standard GR model for which we estimate  $M$ ,  $j$  and  $q$ ; and the extended model where we estimate  $M$ ,  $j$  and  $q$  but allow the individual mode parameters to vary away from their GR predicted values through the  $\Delta\hat{\omega}_{lm}$  and  $\Delta\hat{\tau}_{lm}$  parameters. We shall see that even in the event where a source is too distant to allow the consistency method discussed in the previous section to be applied, it could still be possible to perform model selection to distinguish between GR and non-GR models.

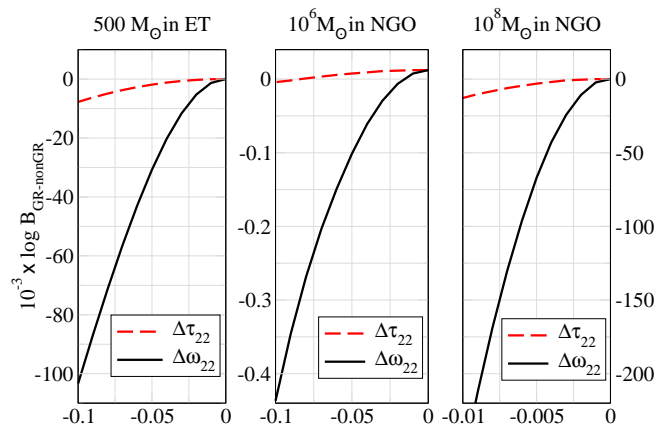


FIG. 7: The differences in evidence between the GR and non-GR models against  $\Delta\hat{\omega}_{22}$  and  $\Delta\hat{\tau}_{22}$  (blue and blue dotted lines respectively). (Top-Left) For injections of  $M = 500$  at 125 Mpc in ET, with SNR between 2664 and 2888. (Top-Right) For injections of  $10^8 M_\odot$  in NGO at 1 Gpc, with SNR between 114909 and 115154. (Bottom) For injections of  $10^6 M_\odot$  in NGO at 125 Mpc, with SNR between 1706 and 1757.

Bayesian model selection is a method of determining, for a given signal, whether the GR or non-GR model is more likely by comparing the evidences for each. Note that unlike in the previous case where we estimated the QNM parameters directly, here we are estimating the physical parameters of the source along with deviations from the QNM parameters, where all QNM parameters are allowed to vary together. The reason for this difference is that in estimating the QNM parameters directly we would not have a corresponding GR model with any free parameters unless we also searched over  $M$ ,  $j$  and  $q$ . Because in the non-GR case we are measuring five parameters, including the best-determined ones, the resulting joint probability distributions are strongly correlated, although the presence of the 21 mode and the assumption that  $\Delta\tau_{33} = 0$  help to break the degeneracy.

Here we compare evidences for both GR and non-GR signals injected into simulated ET and NGO data as described above, but calculate the evidence for each model

using the nested sampling algorithm. The ratio of these evidences, known as the Bayes factor, quantifies the support for one model over the other provided by the data. Full computation of the Bayesian evidence automatically takes into account the difference in dimensionality of the parameter space, which penalises the more complex non-GR model accordingly, as we shall see.

Figure 7 displays how the Bayes factor between the GR and non-GR models changes as the deviation of the injected signal from GR increases. In the case of ET, we used the signal from a  $500 M_\odot$  black hole at a distance of 125 Mpc, giving a signal to noise ratio between 2644 and 2888. The NGO simulation used both a  $10^8 M_\odot$  system at a distance of 1 Gpc, with signal to noise ratio between 114909 and 115154, and a  $10^6 M_\odot$  system at a distance of 125 Mpc, with signal to noise ratio between 1706 and 1757. For ET and the  $10^6 M_\odot$  NGO system, we varied both  $\Delta\hat{\omega}_{22}$  and  $\Delta\hat{\tau}_{22}$  in the range  $-0.1$  to  $0$ , whereas for the  $10^8 M_\odot$  NGO system, we varied  $\Delta\hat{\omega}_{22}$  and  $\Delta\hat{\tau}_{22}$  in the range  $-0.01$  to  $0$ , and in each case computed the evidence for both GR and non-GR models. As the deviation from GR increases, the evidence for the non-GR model increases whilst the evidence for the GR model decreases, causing the Bayes factor (the ratio of evidences for the two models in log space) to increasingly favour the non-GR model, as expected. This is because as the deviation from GR increases, the data fits the GR model with less accuracy, but the parameter freedom of the non-GR model permits a consistency with the data. If we assume a threshold of  $\log B_{GR,non-GR} = -10$  (corresponding to prior odds of  $e^{10}$  in favour of the non-GR model), below which a deviation is considered significant, then with the source parameters above we are able to distinguish deviations at the level of 1% with ET and NGO for the most sensitive  $\Delta\hat{\omega}_{22}$  parameter.

As with the mode resolution of testing GR, the power of the model selection test decreases with increasing source luminosity distance since the signal visibility decreases. The model selection method was carried out for the sources above at distances spanning the entire range outlined in Section IV A, and the Bayes factor between the GR and non-GR minimal set plotted as a function of distance for signals with different deviations from GR. Figure 8 shows that for signals with larger deviations from GR, the maximal set non-GR model is favoured out to much greater distances. We see also that for GR injections, the GR model is indeed preferred, since the simpler model fits the data adequately. When the distance is increased, the size of this effect decreases as the posterior distribution for the modified parameters gradually expands to fill the prior range. The power of the model selection method relies on the ability to exclude parts of the parameter space of the more complex model.

For the purposes of comparison, if we again impose a threshold on the Bayes factor of  $\log B_{GR,non-GR} = -10$ , we see that the non-GR model is favoured above the threshold at all distances for the  $10^8 M_\odot$  system with a deviation of only 0.6%, whereas deviations as small as

0.1% can be detected out to a distance of  $\sim 10.7$  Gpc. For the  $10^6 M_\odot$  NGO system, the non-GR model is favoured above the threshold up to  $\sim 1$  Gpc for a 2% deviation and  $\sim 6$  Gpc for a 10% deviation. For ET, we are able to cross the threshold up to  $\sim 1.61$  Gpc for a 2% deviation and 6.63 Gpc for an 8% deviation.

## V. CONCLUSIONS

In this paper we have investigated how well quasi-normal modes could be used to test general relativity. Our work is based on a quasi-normal mode signal model [17] which assumes that the progenitor binaries are non-spinning. We have specifically looked at the ability of future ground- and space-based detectors in testing the black hole no-hair theorem. More specifically, we have investigated how well future interferometric gravitational wave detectors can test deviations of quasi-normal mode frequencies and damping from their general relativistic values.

As expected, the  $l = 2, m = 2$  mode of the signal is the most clearly measurable for the sources we considered, which can be used to infer the mass and spin of the black hole. Measurement of a third parameter, i.e. the frequency of the  $l = 3, m = 3$  mode, is then used to confirm consistency between the modes. If the true signal is consistent with GR then the measurement of the different parameters would be consistent with one another. We find that a 10% deviation in  $\omega_{22}$  is clearly discernible for a  $500 M_\odot$  source at 1.25 Gpc in ET, as well as  $10^6$  and  $10^8 M_\odot$  sources at 1.25 Gpc and 10 Gpc, respectively, in NGO. Within the reach of NGO, the event rate could be pretty high and so no-hair tests are promising in this case. Binary coalescences of intermediate mass black holes within 1.25 Gpc are highly unlikely and hence ET might not be able to carry out such tests, except in the case of rare close by events.

In Section IV C, therefore, we applied Bayesian model selection to obtain a more robust and quantitative measure of the consistency of the data with GR vs a generalised theory where the mode parameters depended on an extra parameter other than the black hole mass and spin (i.e., ‘hairy’ black holes). Using this technique, we are able to measure deviations at the 10% level in the  $\hat{\omega}_{22}$  parameter out to  $\simeq 6$  Gpc for a  $500 M_\odot$  source with the Einstein Telescope. With NGO, we are able to measure deviations at the 10% level at 6 Gpc with a  $10^6 M_\odot$  source, and the 0.6% level at  $z \sim 5.1$  with a  $10^8 M_\odot$  source.

In the above analysis, we have assumed that the location and orientation of the GW source is known prior to the analysis—a significantly simplified analysis compared to the full problem of determining these parameters alongside the test of relativity. Another limitation of our study is that it is restricted to a small number of systems with very specific source location, orientation and mass ratio of the progenitor binary. Moreover, due to the

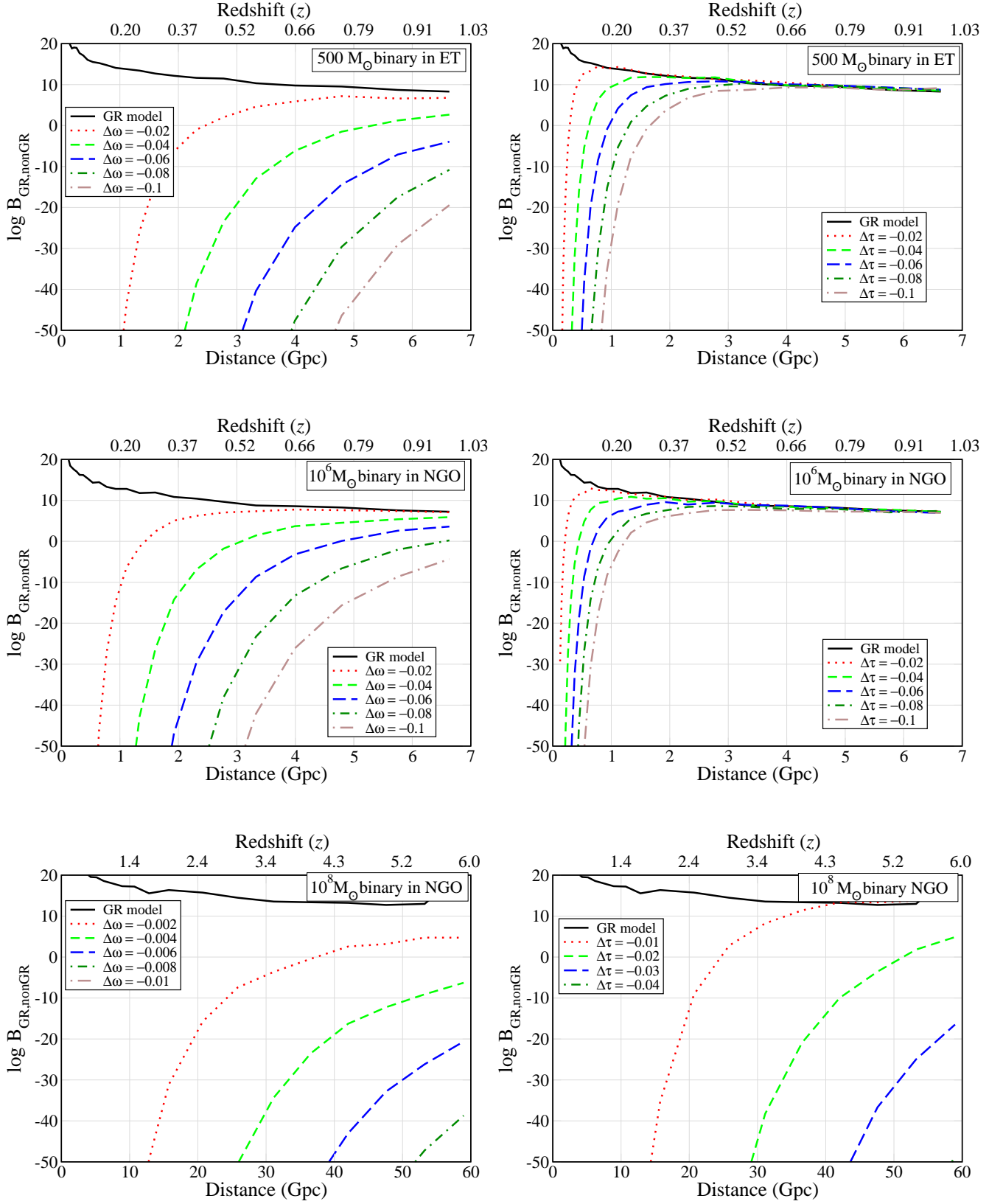


FIG. 8: The differences in evidence for the GR and non-GR models is plotted against the luminosity distance to the source, for observation of ringdown signals from a  $500 M_{\odot}$  black hole in ET (top panels),  $10^8$  and  $10^6 M_{\odot}$  black hole in NGO (middle and bottom panels respectively). The non-GR model is simulated by varying either  $\Delta\hat{\omega}_{22}$  (left panels) or  $\Delta\hat{\tau}_{22}$  (right panels) as compared to their GR values of 0.  $\Delta\hat{\omega}_{22}$  and  $\Delta\hat{\tau}_{22}$  are varied over the range 0 to  $-0.1$  in steps of  $-0.01$  in the case of ET and the  $10^6 M_{\odot}$  NGO system, and over the range 0 to  $-0.01$  in steps of  $-0.001$  in the case of the  $10^8 M_{\odot}$  NGO system, while keeping all other parameters as for GR. The different curves in each panel correspond to different values of the non-GR parameter, starting with 0 for the top most curve and changing by either  $-0.01$  (top and bottom panels) or  $-0.001$  (middle panels). A difference in evidence of  $-10$  or smaller is considered good enough to discriminate a non-GR model from GR model.

lack of accurate models, the study has used a very simple model of the ringdown signal that neglects the effect of initially spinning black holes of the progenitor binary. The presence of spins could significantly alter the spectrum of the modes excited and their relative amplitudes, which could impact our ability to infer the mass ratio of the progenitor binary and the no-hair tests studied in this paper. Nevertheless, the methods we have developed in this work are equally applicable to the more general case, which should be performed as part of a follow-up study. Such a study will be helpful in a more robust evaluation of the potential of future detectors in testing the no-hair theorem.

## VI. ACKNOWLEDGEMENTS

The authors gratefully acknowledge support from the Science and Technology Facilities Council (STFC) UK, grant ST/H002006/1. We would like to thank Ioannis Kamaretsos for his input and advice on the simulations, Ilya Mandel for helpful comments, and the LIGO Data-Grid clusters which allowed us to run the simulations used in this paper.

- 
- [1] J. Abadie et al. (LIGO Scientific Collaboration) (2010), arXiv:1003.2480.
  - [2] B. Abbott et al., Tech. Rep. LIGO-M060056-08-M, LIGO Project (2007), URL <http://www.ligo.caltech.edu/docs/M/M060056-08/M060056-08.pdf>.
  - [3] F. Acernese et al., *Classical and Quantum Gravity* **23**, S635 (2006).
  - [4] L. Blanchet and B. S. Sathyaprakash, *Phys.Rev.Lett.* **74**, 1067 (1995).
  - [5] C. M. Will, *Living Reviews in Relativity* **9** (2006), URL <http://www.livingreviews.org/lrr-2006-3>.
  - [6] B. S. Sathyaprakash and B. F. Schutz, *Living Rev. Rel.* **12**, 2 (2009), arXiv:0903.0338.
  - [7] C. K. Mishra, K. G. Arun, B. R. Iyer, and B. S. Sathyaprakash (2010), 1005.0304.
  - [8] N. Yunes and F. Pretorius, *Phys. Rev. D* **80**, 122003 (2009), 0909.3328.
  - [9] R. Kerr, *Phys. Rev. Lett.* **11**, 237 (1963).
  - [10] C. Vishveshwara, *Nature* **227**, 936 (1970).
  - [11] E. Berti, V. Cardoso, and A. O. Starinets, *Class. Quant. Grav.* **26**, 163001 (2009), 0905.2975.
  - [12] R. Ruffini and J. A. Wheeler, *Physics Today* **24**, 30 (1971).
  - [13] E. W. Leaver, *Proc. R. Soc. Lond.* **402**, 285 (1985).
  - [14] O. Dreyer, B. Kelly, B. Krishnan, L. S. Finn, D. Garrison, and R. Lopez-Aleman, *Class. Quantum Grav.* **21**, 787 (2004), gr-qc/0309007.
  - [15] E. Berti, V. Cardoso, and C. M. Will, *Phys.Rev.* **D73**, 064030 (2006), gr-qc/0512160.
  - [16] E. Berti, J. Cardoso, V. Cardoso, and M. Cavagliá, *Phys. Rev.* **D76**, 104044 (2007), gr-qc/0707.1202.
  - [17] I. Kamaretsos, M. Hannam, S. Husa, and B. S. Sathyaprakash, *Phys. Rev. D* **85**, 024018 (2012), URL <http://link.aps.org/doi/10.1103/PhysRevD.85.024018>.
  - [18] M. Punturo, M. Abernathy, F. Acernese, B. Allen, N. Andersson, et al., *Class.Quant.Grav.* **27**, 194002 (2010).
  - [19] B. Sathyaprakash, M. Abernathy, F. Acernese, P.-S. N. Andersson, K. Arun, et al. (2011), to appear in *Proceedings of the Rencontres de Moriond Meeting, March 20-27, La Thuille, Italy*, gr-qc/1108.1423.
  - [20] M. Davis, R. Ruffini, H. Press, and R. Price, *Phys. Rev. Lett.* **27**, 1466 (1976).
  - [21] E. E. Flanagan and S. A. Hughes, *Phys.Rev.* **D57**, 4535 (1998), gr-qc/9701039.
  - [22] T. Li, W. Del Pozzo, S. Vitale, C. Van Den Broeck, M. Agathos, et al. (2011), 1110.0530.
  - [23] J. Veitch and A. Vecchio, *Phys. Rev. D* **81**, 062003 (2010).
  - [24] LSC Algorithm Library software, see URL: <http://www.lsc-group.phys.uwm.edu/lal>.
  - [25] O. Jennrich, A. Petiteau, and E. Porter, Tech. Rep., The ELISA(NGO) Science Performance Task Force (2011), URL [https://lisa-light.aei.mpg.de/lisa-light/pub/DetectorConfigurations/FinalConfiguration/ELISA-NGO\\_FinalConfig.pdf](https://lisa-light.aei.mpg.de/lisa-light/pub/DetectorConfigurations/FinalConfiguration/ELISA-NGO_FinalConfig.pdf).
  - [26] E. Wright, *The Publications of the Astronomical Society of the Pacific* **118**, 510102 (2006).
  - [27] I. Kamaretsos (2011), 1112.3077.